

Prediction of acoustic field induced by a tidal turbine under straight or oblique inflow via a BEM/FW-H approach

Seungnam Kim* and Spyros A. Kinnas^a

*Ocean Engineering Group,
Department of Civil, Architectural and Environmental Engineering, The University of Texas at Austin,
Austin, TX, 78712, U.S.A.*

(Received December 15, 2022, Revised May 5, 2023, Accepted May 13, 2023)

Abstract. This study investigates the influence of loading and inflow conditions on tidal turbine performance from a hydrodynamic and hydroacoustic point of view. A boundary element method is utilized for the former to investigate turbine performance at various loading conditions under zero/non-zero yaw inflow. The boundary element method is selected as it has been selected, tested, and validated to be computationally efficient and accurate for marine hydrodynamic problems. Once the hydrodynamic solutions are obtained, such as the time-dependent surface pressures and periodic motion of the turbine blade, they are taken as the known noise sources for the subsequent hydroacoustic analysis based on the Ffowcs Williams-Hawkings formulation given in a form proposed by Farassat. This formulation is coupled with the boundary element method to fully consider the three-dimensional shape of the turbine and the speed of sound in the acoustic analysis. For validations, a model turbine is taken from a reference paper, and the comparison between numerical predictions and experimental data reveals satisfactory agreement in hydrodynamic performance. Importantly, this study shows that the noise patterns and sound pressure levels at both the near- and far-field are affected by different loading conditions and sensitive to the inclination imposed in the incoming flow.

Keywords: boundary element method; Ffowcs Williams-Hawkings (FW-H) formulation; hydroacoustics; marine current turbine; renewable energy

1. Introduction

In recent years, interest in the energy harvesting system from water resources has been growing because of the need for clean and renewable energy. Among many different types of energy generators based on tidal stream, the horizontal axial tidal turbine has been most frequently installed over the globe because of its high efficiency, similarity to wind turbines, and the analysis tools that were initially developed for propellers but equally applicable to turbine problems without extensive modifications in numerical aspects. Because of the predominantly oblique flow about the turbine axis in most tidal current sites, typical turbine arrangements are subject to unsteady forces on the blade. The potential impacts of the unsteadiness on turbine performance thus need to be studied to understand the overall turbine efficiency in either a single or farm arrangement.

*Corresponding author, Postdoctoral Fellow, E-mail: naoestar@utexas.edu

^aProfessor, E-mail: kinnas@mail.utexas.edu

Previous research has been performed on the hydrodynamic and hydroacoustic performance of tidal turbines. For the former, Kim *et al.* (2021) applied a boundary element method (BEM) to a single turbine problem to predict its performance in the presence of cavitation. Later, they coupled BEM with a Reynolds-averaged Navier-Stokes (RANS) solver to multiturbine problems with different layouts to investigate the potential impact of downstream wake on the energy-shadow effect of the turbines located inside the downstream wake. Baltazar & Falcão de Campos (2011) also applied a low-order panel method to analyze the flow around a horizontal axis marine turbine. They showed that the helicoidal wake model parameters used in the analysis significantly impacted the turbine performance and discussed the effect of viscosity that explains the main discrepancies within numerical data. Menéndez Arán *et al.* (2019) used a lifting line model approach to determine the optimum loading on the turbine blade. Importantly, they discussed the influence of the wake alignment model and its geometry on the distribution of the turbine blade loading and corresponding power coefficients under different numbers of the blade and tip speed ratios. Young *et al.* (2010) developed a coupled BEM-finite element method to simulate the transient fluid-structure interaction response of tidal turbines under spatially varying inflow. They revealed that the blades would undergo excessive deformation because of the high fluid loading and slender blade profile. Otto *et al.* (2012) showed that the effect of viscosity turned out to be very relevant to the performance of the model turbine discussed in their paper, making BEM applications to the turbine problem quite challenging numerically. Flow separation on the suction side of the turbine blade at high loading typically induces significant drops in the turbine performance that the inviscid BEM cannot correctly handle unless otherwise corrected numerically.

Compared to a number of acoustic analyses performed on the wind turbine grounded or offshore installed, it is relatively hard to find previous publications that discuss noise predictions or measurements from a similar energy harvesting system, the marine current turbine. Literature reviews reveal somewhat limited data on numerical predictions of tidal turbine noise, despite its practical and beneficial interest raised by multidisciplinary research. The main difficulty might originate from a pure difficulty in measuring high-fidelity underwater noise inside harsh ocean environments. Lloyd (2013) and Lloyd *et al.* (2014) performed a model-scale tidal turbine simulation using large eddy simulations (LES) to investigate the unsteady blade loading and noise radiation from the turbine. They showed that the dominant noise sources are concentrated at the blade leading edge towards the tip. The inflow turbulence was considered, and acoustic radiation was estimated using a compact source of the Ffowcs Williams-Hawkings (FW-H) equation. Shi *et al.* (2016) studied cavitating and underwater noise performance of a horizontal-axis tidal turbine.

They especially modified the leading-edge design with the tubercles on the pectoral fins of humpback whales. The leading-edge tubercles triggered the cavity inception earlier but constrained the cavity region between tubercles, thus affecting the noise performance. Lossent *et al.* (2018) assessed the acoustic impacts of tidal turbines on marine life. They measured the noise source using 19 drifting transects at distances between 100 m and 2400 m from the turbine. The acoustic footprint revealed that behavioral disturbance of fishes and marine mammals might occur up to 1 km around a single turbine. They pointed out that more concerns would be on the noise from a farm with up to 100 turbines. In response to the environmental concern of current energy converters to marine life, a commercial-off-the-shelf hydrophone was deployed in a free drifting configuration to measure underwater noise from a tidal turbine, and the corresponding results were reported in Haxel *et al.* (2022). Results from this research showed that acoustic noise from the tidal turbine was below the ambient noise level; therefore, it does not significantly affect the underwater noise levels of the project site. A similar conclusion was drawn by Lloyd *et al.* (2014) in that the derived noise from turbines is not expected to cause a physical impact on fish. Risch *et al.* (2020) focused on the underwater sound emitted by a 1.5 MW three-bladed horizontal axis tidal turbine in the Pentland

Firth, Scotland. The turbine emissions elevate noise levels by about 30 to 40 dB above the ambient noise in low sea states, making the signal measurable at ranges of over 2000 m from the turbine. They found that the sound levels are linked to the turbine RPM and current speeds. In the work of Schmitt *et al.* (2015), the authors pointed out that the effect of turbine noise cannot be assessed as a stand-alone issue, but rather should be investigated in the context of natural background noise in high-flow conditions. They presented sound measurements from a testing campaign performed at the tidal test site in Portaferry to propose possible applications as a monitoring system.

2. Objectives

In this article, a BEM/FW-H approach is applied to investigate the overall performance of a tidal turbine. The primary purpose is to see how the loading condition and inflow direction affect the hydrodynamic and hydroacoustic performance of the model turbine taken from the famous Southampton turbine experiment (Bahaj *et al.* 2007). Ideally, the turbine performance must be appreciated within the context of practical current scenarios, including oscillating flow, oblique flow, and potential cavity inception in the form of partial- or supercavitation. However, it is also a practical interest to simplify the problem such that the turbine unit is subject to uniform inflow with possible yaw but in the absence of any upstream geometry. This assumption is valid for front-line turbines sitting upstream in a turbine farm and allows steady and uniform inflow where inflow turbulence is not as significant. By simplifying the problem down to nearly open water conditions, it might be better understood how the loading condition or inflow direction affects the turbine performance without considering vortical interactions with other structures.

A BEM/FW-H approach is adopted in this study because of its fast and accurate prediction of turbine performance, as well as its *linear* noise (the quadrupole noise term is not considered in this study). The noise patterns around the turbine will be predicted at near- and far-field with full consideration of the time travel of sound at underwater speed. This method has been previously developed and successfully applied to marine propeller problems (e.g., single/multi propellers, in both the open water/ship behind conditions) in the past (Seol *et al.* 2002, Testa *et al.* 2018, Ebrahimi *et al.* 2019, Götttsche *et al.* 2019, Kim and Kinnas 2022b, c). In the case of turbine problems, however, relatively few discussed the BEM/FW-H approach for their acoustic problems, even though the same philosophy adopted for propeller applications can be readily extended to the turbine blade without extensive modifications in numerical implementation – the tidal turbine has many things in common with the primary mechanism of marine propellers. The weakness of the present method has to be pointed out in terms of the viscous noise associated with flow separation or downstream turbulence, which falls outside the scope of the present work. Nonetheless, if we confine our interest in the linear noise evaluated away from the downstream wake, the present method might be sufficient and useful to handle tonal noise that contains primary acoustic energies.

3. Methodology

3.1 The hydrodynamic boundary element method (BEM)

A boundary element method (BEM or panel method), over the past decades, has been adopted/tested/validated for many different types of marine propulsors for the predictions of

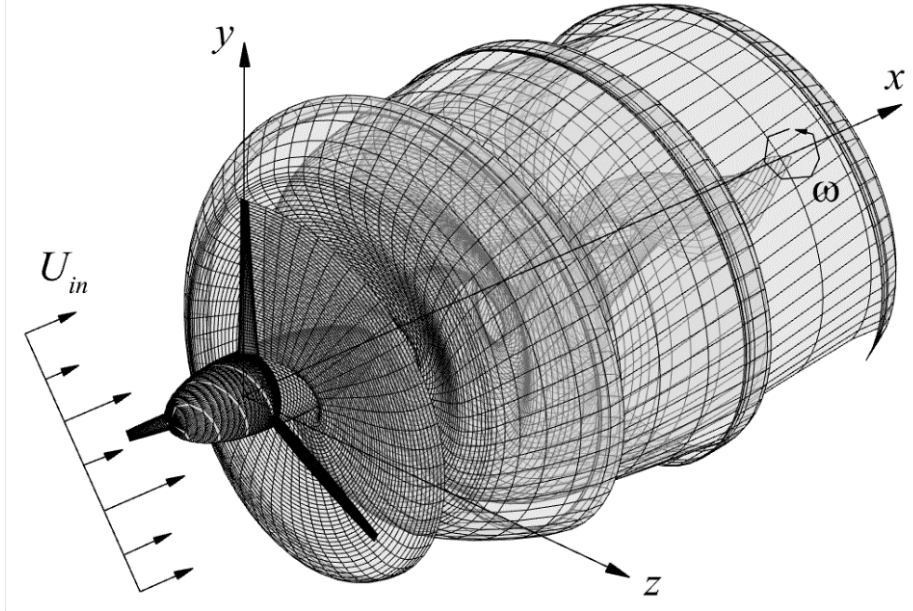


Fig. 1 Turbine geometry with its wake from the key-blade[†] subject to the general inflow, modeled by the hydrodynamic BEM; the x , y , and z axes represent the turbine fixed coordinate system

steady/unsteady performance of open/ducted configurations in fully-wetted/cavitating flow mainly under open water condition and partially in ship-behind condition. This section will briefly touch on the core of the method applied to the hydrodynamic analysis of a tidal turbine (Kim *et al.* 2021, 2023).

In the turbine problem solved by the hydrodynamic BEM, the total flow field \vec{q} is decomposed into the incoming flow \vec{U}_{in} (Fig. 1) given as the general (effective) inflow, rotational component of the blade, and perturbation velocity \vec{u} due to the presence of the turbine in an inviscid and irrotational flow

$$\vec{q} = \vec{U}_{in} - \vec{\omega} \times \vec{r} + \vec{u} \quad (1)$$

The perturbation velocity \vec{u} can be obtained by taking a gradient on the solution velocity potential ϕ that satisfies the Laplace equation

$$\vec{u} = \nabla\phi \quad (2)$$

$$\nabla^2\phi = 0 \quad (3)$$

The perturbation potential on the turbine surface S_T can be expressed as a superposition of the potentials induced by a continuous source and dipole on S_T , as well as a continuous dipole distribution on the trailing wake S_W . Based on Green's third identity, the velocity potential ϕ at point p on the turbine surface should satisfy the following

[†] In the hydrodynamic BEM code, the problem is solved over one blade, the “key” blade, with the effects of the other blades accounted for once (steady problem) or in an iterative sense (unsteady problem).

$$2\pi\phi_p = \iint_{S_T} \left[\phi_q \frac{\partial G(p;q)}{\partial n_q} - G(p;q) \frac{\partial \phi_q}{\partial n_q} \right] dS + \iint_{S_W} \Delta\phi_W \frac{\partial G(p;q)}{\partial n_q} dS \quad (4)$$

where $G(p;q) = 1/R(p;q)$ is Green's function; $R(p;q)$ the distance between control point p and variable point q ; n_q the unit normal vector pointing into the fluid; and $\Delta\phi_W$ is the potential jump across the wake surface. To secure the uniqueness of the solutions, the kinematic boundary condition is applied to provide the unknown source strength on the turbine surface. Once the unique solutions are obtained, the turbine-induced velocity (Eq. (2)) can be evaluated anywhere in the flow field by taking a gradient on the solution potential.

There are many ways to model the turbine trailing wake (Kim *et al.* 2022a) developed to predict the turbine performance accurately. Among the models, this work will adopt the full wake alignment (FWA) scheme that has been developed basically for steady run under uniform inflow. This model has been proven to be the most accurate as it fully represents the development of downstream wake by aligning the wake panels onto the local stream induced by the turbine and the wake itself (note that wake panel edges are concentrated vortices detached from the blade trailing edge) without any simplification on the wake geometry. Figure 1 shows the model turbine with a fully aligned wake via FWA. It is shown that rollups at the wake tip are well-represented by the wake panels.

To consider the effect of viscosity, the present method applied a viscous pitch correction using an empirical correction to the pitch angle of the turbine blade, and a constant friction coefficient (C_f) over the blade surface to account for the friction forces, as proposed by Kerwin and Lee (1978). Another possible way, which is not implemented in this paper, is to couple the present panel method with a two-dimensional (2D) boundary layer solver (called X-Foil), modified to account for the effects of 3D, applied along each blade strip and its wake, with the effects of the other strips on the same and the other blades being included in an iterative sense (Kinnas *et al.* 2012, Wu *et al.* 2023).

As will be shown in the result section, the present method, without the empirical viscous pitch correction and a constant C_f , predicts the turbine force quite well but significantly overpredicts the turbine efficiency.

3.2 Acoustic analysis of a tidal turbine by a BEM coupled with the FW-H formulation

For the noise prediction radiated from the tidal turbine, the present method adopts the solutions of an inhomogeneous wave equation, the Ffowcs Williams-Hawkings (FW-H) formulation (Ffowcs-Williams and Hawkings 1969) in the form proposed by Farassat (Farassat 1A formulation, Farassat 2007) as shown in Eqs. (5) and (6)

$$4\pi p'_T(\vec{x}, t) = \int_{f=0} \left[\frac{\rho_0 v_n}{r(1-M_r)^2} + \frac{\rho_0 v_n \hat{r}_i \dot{M}_i}{r(1-M_r)^3} \right]_{ret} dS \quad (5)$$

$$+ \int_{f=0} \left[\frac{\rho_0 c v_n (M_r - M^2)}{r^2 (1 - M_r)^3} \right]_{ret} dS,$$

$$\int_{f=0} \left[\frac{\dot{p} \cos \theta}{c_0 r (1 - M_r)^2} + \frac{\hat{r}_i \dot{M}_i p \cos \theta}{c_0 r (1 - M_r)^3} \right]_{ret} dS \quad (6)$$

$$+ \int_{f=0} \left[\frac{p(\cos \theta - M_i n_i)}{r^2 (1 - M_r)^2} + \frac{(M_r - M^2) p \cos \theta}{r^2 (1 - M_r)^3} \right]_{ret} dS$$

where p'_T and p'_L denote the acoustic pressures due to the thickness and loading noise, respectively.

The summation of the two terms produces the total linear pressure p' (the nonlinear term is not considered since it requires volume information across the flow, which is not feasible in a surface integral method).

$$p'(\vec{x}, t) = p'_T(\vec{x}, t) + p'_L(\vec{x}, t) \quad (7)$$

p here represents the *gauge* pressure[‡] on the blade surface S ; r the distance between the source and observer \vec{x} positions; ρ_0 the medium density; $M_r = \vec{v} \cdot \hat{r}/c_0$ the Mach number in the direction of radiation \hat{r} ; \vec{v} the surface velocity of the blade; $\cos \theta = n_i \hat{r}_i$ with θ the local angle between the surface normal vector n_i and radiation direction \hat{r}_i at the noise emission time τ_e . The subscription *ret* emphasizes that the kernel functions of each integral are time retarded with compressibility delay and evaluated at τ_e when solving the integrals over the impermeable blade surface $f = 0$ at real-time t . The dot over a variable means the source time derivative of the variable at the emission time. Eqs. (5) and (6) are written separating the near-field terms (in the order of $1/r^2$) from the far-field terms (order of $1/r$). If the geometry of a rotating blade, its trajectory in time, and the surface loadings are known a priori via a separate hydrodynamic analysis, the integral representations can be solved for the acoustic pressures propagating from the turbine blade to anywhere in the flow field at the speed of sound.

4. Results and discussions

4.1 The model turbine and its hydrodynamic performance

Before the acoustic analysis, this section presents the model turbine from the reference experiment and its hydrodynamic performance investigated by BEM. For validations, comparisons are also made with available experimental data for various loading/inflow conditions. This validation is crucial since the predicted performance will be the known noise source in the following acoustic analysis (Section 4.2). The model turbine (Fig. 2) is taken from Bahaj *et al.* (2007), which has been adopted/tested/validated by a number of researchers because of its well-documented and abundant data in both wetted and cavitating conditions. The model geometry is given as a three-bladed marine current turbine with a horizontal axis and tested in the cavitation tunnel over a wide range of tip speed ratios (TSRs) with/without yaw in the incoming flow.

$$\text{Tip Speed Ratio (TSR)} = \frac{\omega R}{V_s} = \frac{\pi n D}{V_s} = \frac{\pi}{J_s} \quad (8)$$

where ω is the turbine angular speed [rad/s]; n the turbine rotational frequency [1/s]; $D = 2R$ the turbine diameter [m] with R being the blade radius; and V_s is the inflow speed far upstream [m/s]. J_s is the advance ratio defined as

$$J_s = \frac{V_s}{nD} \quad (9)$$

The objective of the experiment was to acquire reliable measurements of the power and thrust performance under various loading conditions. The experiment also investigated the cavitation performance, and its comparison with BEM predictions was presented in the authors' previous

[‡] It is the variation from the mean pressure that brings an acoustic signal in the medium; thus, the gauge pressure is used instead of the absolute pressure.



Fig. 2 The model tidal turbine in the cavitation tunnel experiment, taken from Bahaj *et al.* (2007)

publication (Kim *et al.* 2021). Cavitation essentially has been shown to produce broadband noise that can be critical to the communication mechanism of marine species. Despite its importance in underwater acoustics and the capability of the present method in cavity modeling, this paper will skip the cavity prediction and its associated noise in order to focus on turbine noise in fully wetted condition, in which neither cavitation nor the upstream body that brings significant non-uniformity in inflow is present. As it is first attempted to extend the present method to the turbine noise, the main focus will stay within the fully wetted condition, leaving the cavity problem as a future task.

The section profiles of the turbine blade are interpolated from five different 2D profiles, i.e., NACA 63-812 (at the tip), NACA 63-815, NACA 63-818, NACA 63-821, and NACA 63-824 (at the hub). The last two digits stand for the ratio of the maximum thickness to chord length. There is a 15° difference in the pitch between the hub and tip; therefore, 25° hub pitch, for instance, corresponds to 10° *set angle* at the blade tip. The radial distributions of chord, thickness, and pitch are provided in the reference paper (see Bahaj *et al.* 2007).

In the test results, 0° inflow yaw is given for both the 20° and 25° hub pitch cases, and 15° and 30° yaws for the 25° hub pitch case. In the case of non-zero yaw, the BEM problem has to be dealt with in unsteady mode as the forces acting on the key-blade are no longer constant with the blade angle. In the following hydrodynamic or hydroacoustic analysis, the unsteadiness (if any) only comes from the changes in the blade angle in space, not with time at a specific point on the blade. For a given tunnel speed and turbine rotational frequency, the power coefficient (C_{POW}) and force coefficient (C_F) are measured based on the predicted steady/unsteady force F and torque Q following the equation

$$C_F = \frac{F}{\frac{1}{2}\rho V_s^2 A} \quad (10)$$

$$C_{POW} = \frac{Q\omega}{\frac{1}{2}\rho V_s^3 A} \quad (11)$$

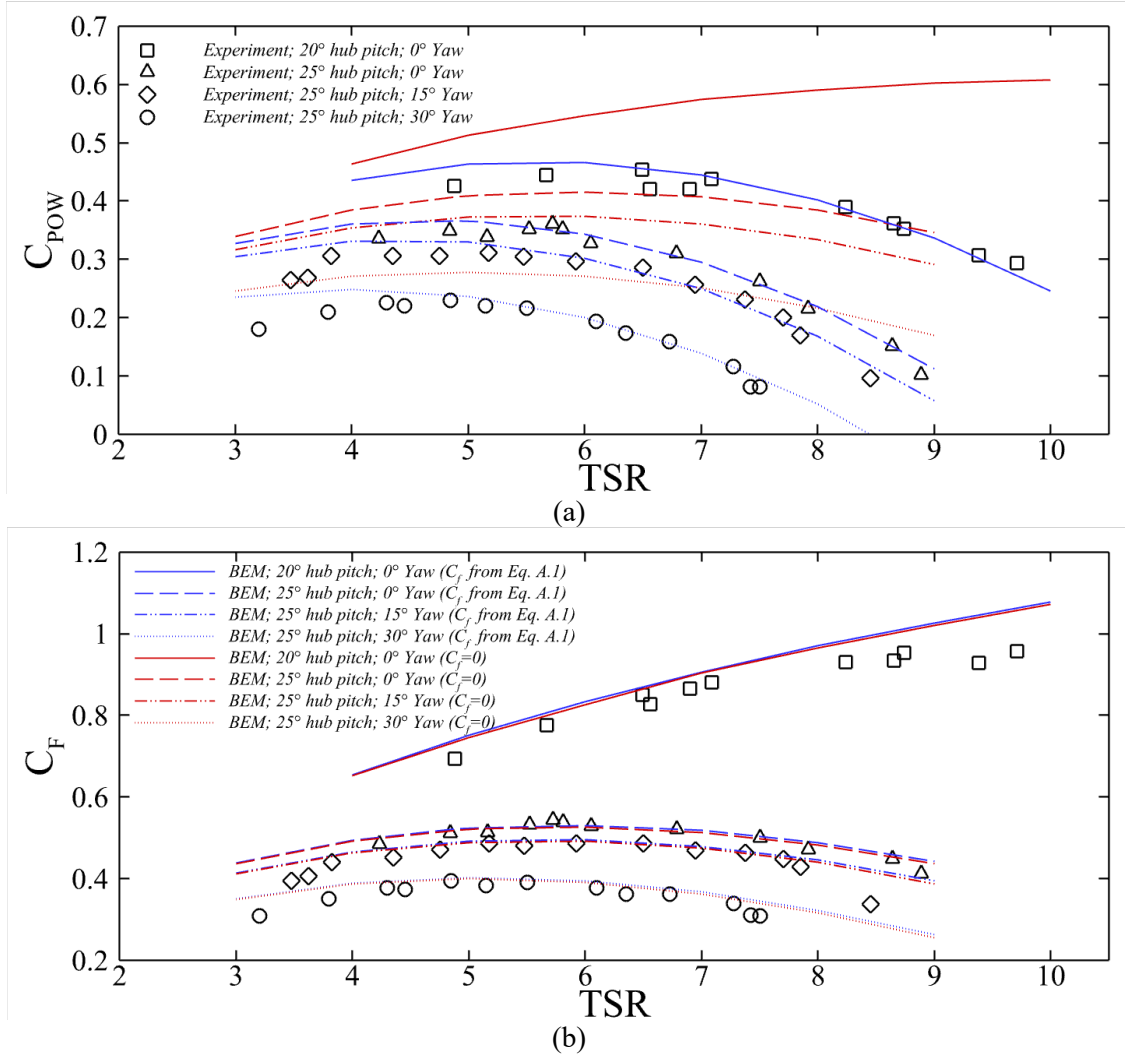


Fig. 3 Hydrodynamic performance of the model turbine (a) C_F and (b) C_{POW} in various testing conditions

where $A = \pi R^2$ [m^2]. Fig. 3 below shows the open water performance of the model turbine predicted by the hydrodynamic BEM in comparison with experimental data. Two different pitch setups are investigated in fully-wetted condition. A constant friction coefficient $C_f = .008^{\S}$ is applied over the blade surface to account for the viscous effect numerically. 50×20 panels are utilized to discretize the blade surface in the chordwise \times spanwise directions, respectively (see Fig. 1).

Over the tested TSRs in Fig. 3, the wetted results correspond well to the experimental measurements, except for two extreme conditions (i.e., very low or high TSRs). Such a difference

[§] Determination of C_f based on the ITTC-1957 friction correlation line is presented in Appendix.

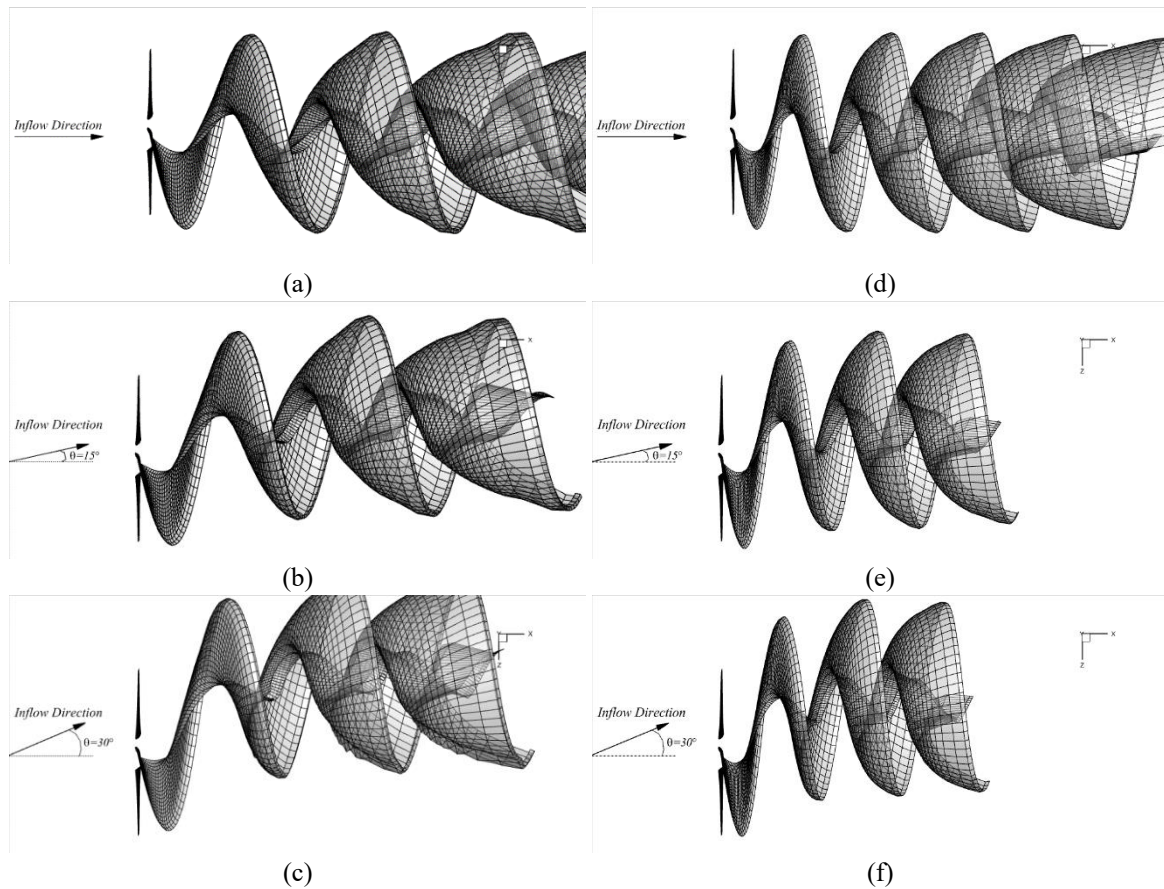


Fig. 4 Predicted turbine wake from the present method with (a),(d) 0°, (b),(e) 15°, and (c),(f) 30° yaw in the incoming flow; hub pitch=25° and TSR = (a)-(c) 4 and (d)-(f) 6

is typical for BEM predictions as for very low TSRs, for example, BEM cannot capture separation on the suction side of the blade due to its inherent inviscid foundation. Separation on the blade, once it appears due to high-speed inflow relative to the rotational speed of the turbine, lowers the surface pressure on the suction side and thus the axial forces. As the present method cannot capture such viscous phenomena, it normally overpredicts the turbine performance at very low TSRs, as shown in the comparison. At very high TSRs, on the other hand, the trailing wake becomes extremely compact in space, so more panels will be placed near the blade trailing edge. Since the BEM wake panels cannot represent the diffusion effect downstream, very compact panel arrangements close to the turbine could incorrectly affect the turbine performance creating numerical deviations from physical reality. Due to the same reason, BEM also shows poor performance for very low hub pitch (the 20° case) as it imposes a high angle of attack on the blade and shortens the axial length of the downstream wake. Given that the design loading for the model turbine is set to TSR = 6, the excellent agreement between the experimental and numerical approaches found at this condition seems encouraging. Since the poorly predicted force performance could mean that the noise will also be poorly predicted, the following noise predictions will only be based on TSR = 4~8 which relatively produce satisfactory agreement between BEM and the experiment.

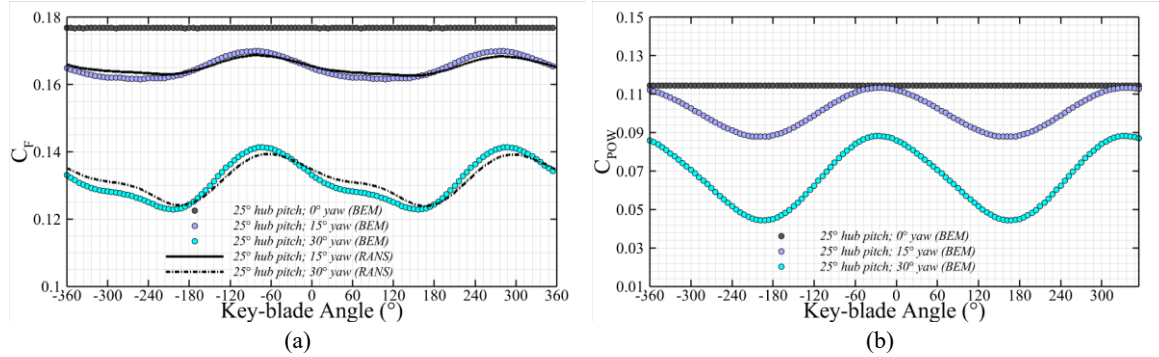


Fig. 5 Steady/unsteady (a) C_F and (b) C_{POW} acting on the key blade under different inflow yaw; 25° hub pitch and TSR = 6

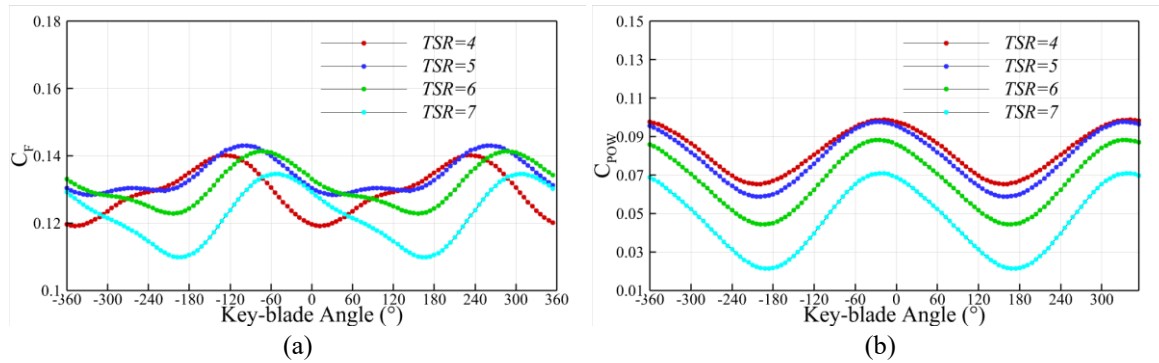


Fig. 6 Unsteady (a) C_F and (b) C_{POW} acting on the key blade under different TSRs; 25° hub pitch and 30° inflow yaw

It is worth noting that when the effect of viscosity is considered by using an empirical pitch correction on the blade and a constant C_f over the blade, the C_{POW} correlation with the experiment improves significantly especially toward the high TSRs, while C_F is not much affected as C_{POW} . It is because the friction force easily dominates the pressure force as the rotational speed of the blade increases, while the impact of surface friction on the latter is usually minimal.

Fig. 4 shows the wake geometries predicted by the present method for TSR = 4 and 6. The directions of the fully aligned wakes are toward the inflow direction, which is no longer parallel to the turbine axis in non-zero yaw cases. During the wake alignment procedure, wake panels might not be fully aligned to the inflow yaw because of their gradual alignment process. The greater the distance from the blade trailing edge, the more computations are required for downstream wake panels as they need to complete additional revolutions to be fully aligned to the local stream. However, the wake panels located far downstream normally do not affect the final solution as much because the dominant wake effects on the turbine performance (propeller as well) mainly come from the near wake close to the turbine in the axial direction. The same panel number is assumed in the downstream wake for both TSRs, but the high TSR case brings the wake panels closer to the turbine in the axial direction due to its high-speed revolution than the lower TSR case. Overall, the wake panels are shown to be reasonably aligned to the inflow direction and local downstream for the given testing conditions. Albeit the turbines mounted in areas of variable flow direction can be made to

swivel to be adapted to inflow direction, this study assumes a fixed turbine axis regardless of the inflow yaw (Fig. 4). It is related to the design aspects of the turbine, which falls outside the scope of the present study.

The unsteady turbine force coefficient C_F and power coefficient C_{POW} are shown in Fig. 5. The force predictions at this particular loading condition were already validated in Kim *et al.* (2021) against the C_F predictions from RANS and are shown here again. As the difference between BEM and RANS falls within 2.4%, and they show quite similar unsteady patterns in C_F , it is reasonable to use the BEM results for noise source in the following noise predictions. The peak values of each force happen with 360° period and 120° shift between adjacent blades; so, all three blades, once combined, would produce almost constant force. It seems that the 30° yaw case predicts higher frequency in C_F than the 15° yaw case because of the increased unsteadiness with the yaw angle. It is also shown that the key-blade produces the maximum efficiency when it passes the top position ($\theta = 0^\circ$) and minima when passing nearly the bottom end ($\theta = \pm 180^\circ$). This trend is observed in common for all other cases with different TSRs (Fig. 6(b)) and is because the rotation direction of the blade at its bottom position becomes opposite to the direction of the incoming flow. This also explains why the mean values of C_{POW} decrease with the yaw angle in inflow (Fig. 3). The force coefficient (C_F), however, does not seem to follow the same trend, and instead, its minima/maxima shift and appear at different angular positions as TSR varies (Fig. 6(a)). It is because reversed pressures appear and affect the blade loading close to the leading edge at high TSRs. Under the uniform inflow with zero yaw, all the unsteadiness disappears, and all blades are now subject to a constant force regardless of their angular positions.

4.2 Hydroacoustic performance of the model turbine with/without yaw

For the noise prediction using the model turbine, the acoustic pressures (turbine-induced pressure fluctuation without the mean) are recorded on numerical transducers sitting around the turbine with 0.1° angular distance between neighboring transducers, as shown in Fig. 7 and its subframe. In total, 3600 transducers are placed along each circle shown in the figure to plot noise directivity at two different radial distances from the turbine center (i.e., $r/R = 2.0$ and 12.0) as near- and far-field predictions, respectively. The turbine axis is aligned to the global x axis, from which the directivity angle starts and increases counterclockwise when viewed from the top (Fig. 7).

Figs. 8 to 11 show the predicted noise directivity at two different radial locations. The overall sound pressure level (OASPL) in the figure is calculated following the equations

$$OASPL = 10 \log_{10} \left(\sum_{i=1}^{n_{SPL}} 10^{\frac{SPL_i}{10}} \right) \text{ dB} \quad (12)$$

$$SPL = 20 \log_{10} \left(\frac{p'}{p_{ref}} \right) \text{ dB} \quad (13)$$

where p_{ref} is the reference pressure in the water medium ($1.0 \mu\text{Pa}$) and n_{SPL} is the total number of sound pressure levels (SPLs) considered over the noise spectra. At the far-field (Fig. 8), the higher pitch case (25° blade pitch) is shown to produce less noise in almost all directions around the turbine than the lower-pitch case (20° blade pitch). The results look corresponding to the force performance in Fig. 3 since higher loading on the blade normally induces higher noise under the uniform inflow.

Under the uniform inflow, different TSRs bring noticeable impact mainly in the upstream and downstream directions ($\theta = 0^\circ$ and 180°) with about a 10 dB difference, while relatively less in

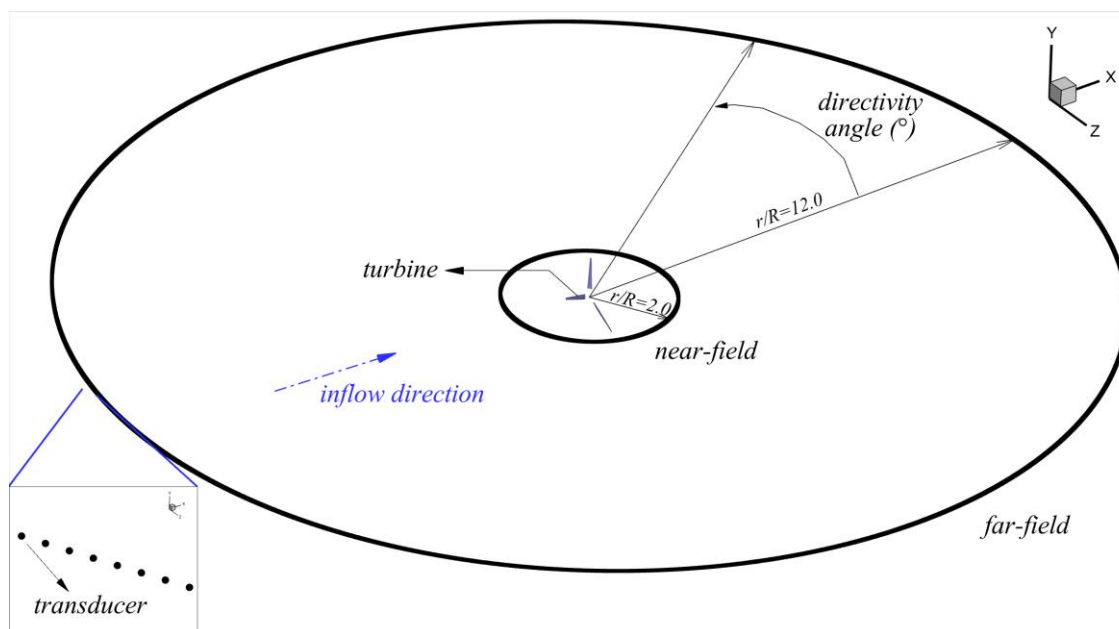


Fig. 7 Numerical transducers placed around the turbine at $r/R = 2.0$ (near-field) and $r/R = 12.0$ (far-field); note that the turbine center is located at the origin

the lateral directions ($\theta = 90^\circ$ or 270°). It is because the turbine blade has a relatively thinner sectional profile and shorter chord length compared to the propeller blade. Looking back on the C_F of the 25° blade pitch case with zero yaw, the magnitude of the blade loading seems to be relatively constant over TRSs compared to the 20° pitch case, and this fact is also well reflected in the overall magnitude of the noise directivity with different TSRs (Figs. 8(a) and 8(b)).

It has to be mentioned that those predictions could be different from physical reality near the downstream direction ($\theta = 0^\circ$) as the present method does not consider the nonlinear noise associated with downstream turbulence or wake dynamics.

The 15° yaw case (Fig. 8(c)) seems to produce similar noise patterns as the 0° yaw case with the same pitch (Fig. 8(b)), but the overall noise levels are increased due to the unsteadiness included in the non-zero yaw problem. The unsteady loading on the blade usually increases the noise level compared to that of a steady problem, and this fact is well reflected in the directivity. As opposed to the previous steady problems, high TSRs now decrease the overall noise. Interestingly, the inclination in the incoming flow significantly affects noise patterns, mainly on the starboard side ($\theta = 0^\circ \sim 180^\circ$), while the port side noise ($\theta = 180^\circ \sim 360^\circ$) is not much affected by any change in TSR. As the yaw angle increases, the problem will experience more unsteadiness (Fig. 5(a)), which brings higher noise in almost all directions (Fig. 8(d)) around the turbine. Fig. 9 shows that the total noise p' mainly comes from the loading noise p'_L even in the steady problems in the present linear predictions, and the contribution of the thickness noise p'_T to p' is quite minor in all cases. Since p'_T is determined by the periodic motion of the blade, its magnitude should not be affected by the inflow condition as predicted; changing TSR or blade pitch could make a difference in p'_T .

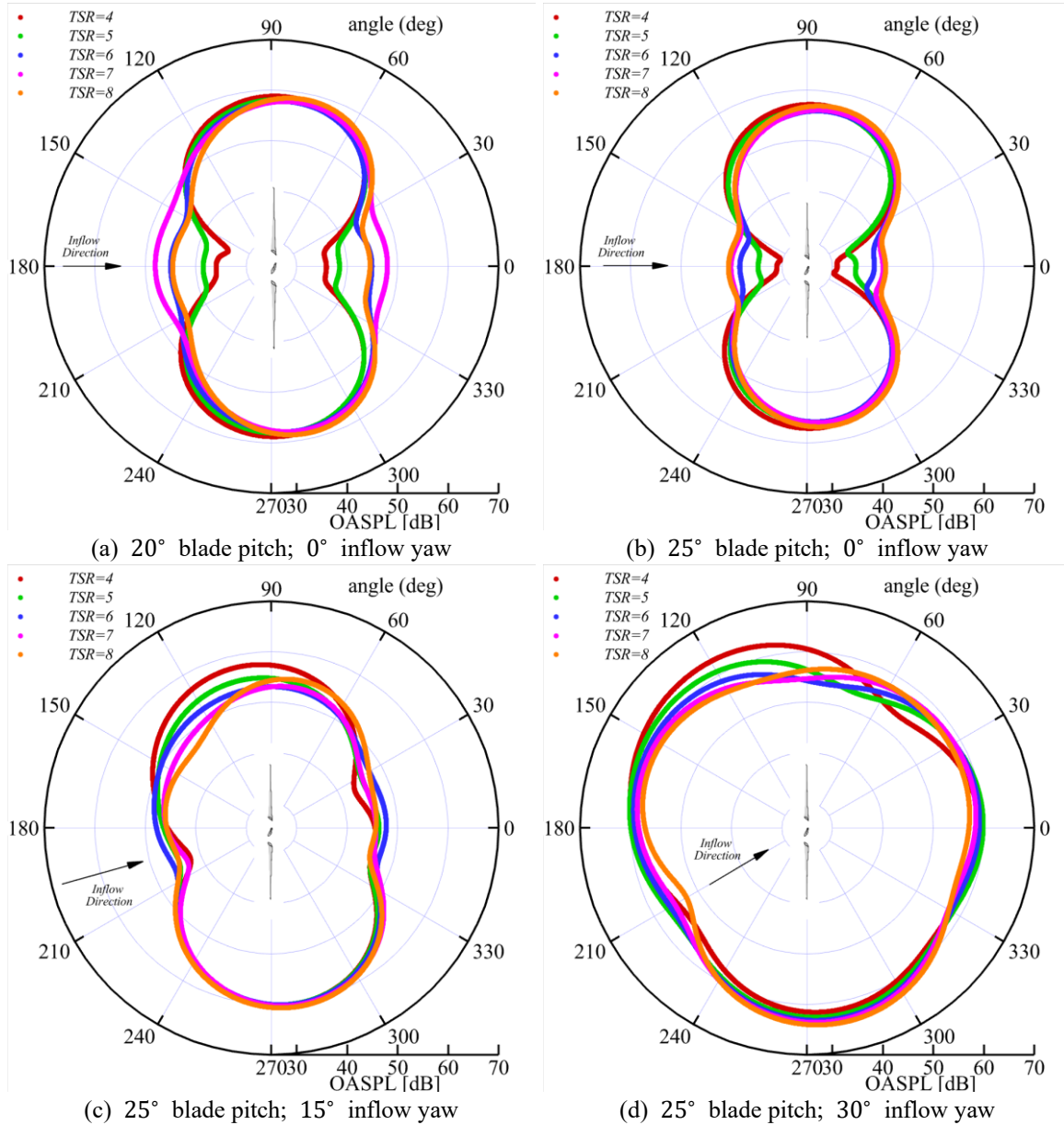


Fig. 8 Noise directivity on the horizontal plane ($y/R = 0.0$) at several TSRs ($c_0 = 1,500$ m/s); pressure transducers are sitting around the turbine at $r/R = 12.0$

Now in Fig. 10, the noise directivity is predicted based on the near-field noise ($r/R = 2.0$). Unlike the far-field noise, the directivity shows clear *butterfly* patterns with more noise toward the downstream than the upstream. Since the turbine blade has negative camber as opposed to the thrusting propeller blade, the turbine blade could induce more noise toward the downstream region than upstream. The overall noise patterns behave quadrupole characteristics which become more distinct as TSR increases. Interestingly, more noise is produced in the side directions than in the

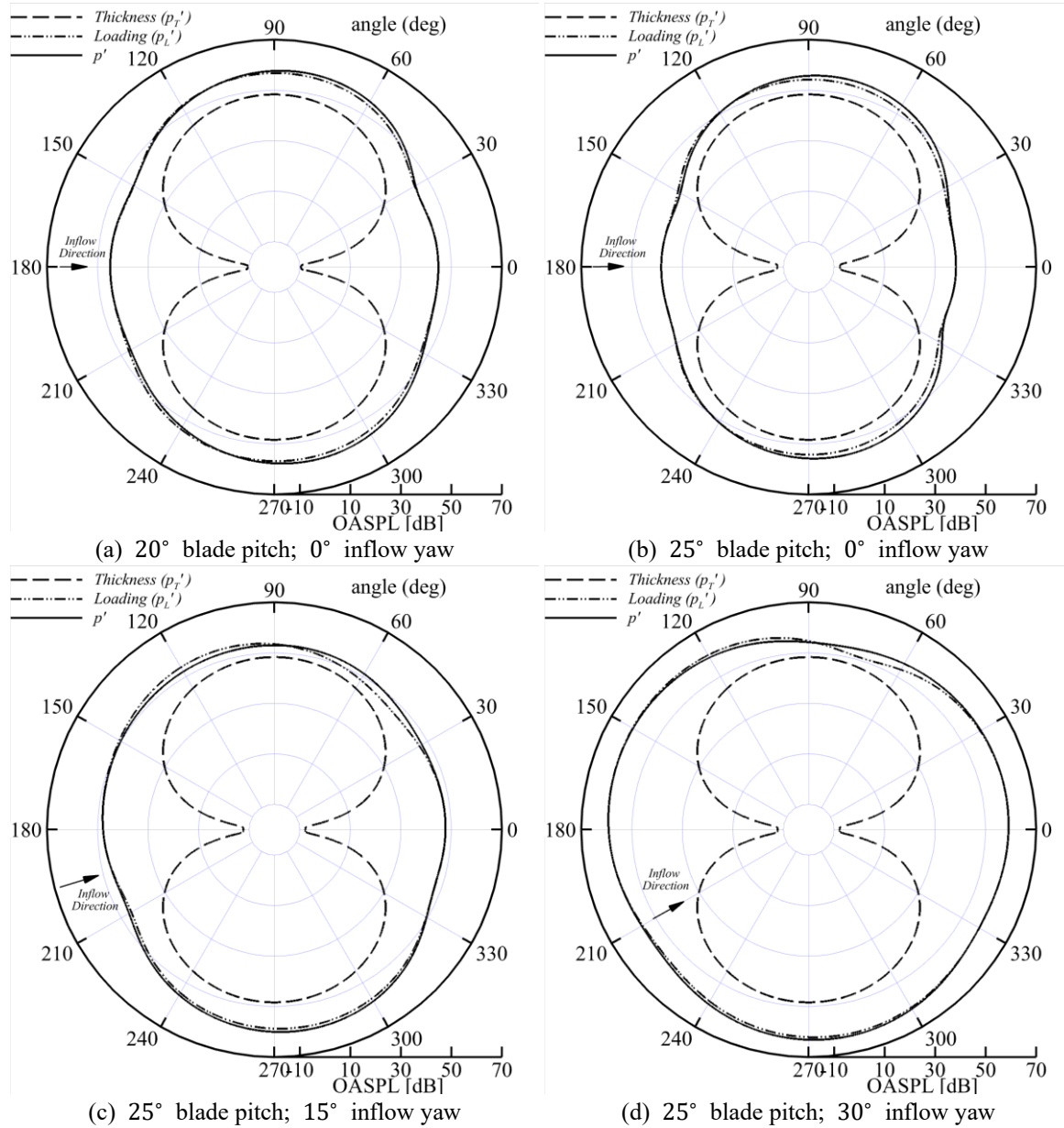


Fig. 9 Noise directivity on the horizontal plane ($y/R = 0.0$) for p'_T , p'_L , and p' at $TSR = 6$ ($c_0 = 1,500$ m/s); pressure transducers are sitting around the turbine at $r/R = 12.0$

front and back directions, even in unsteady cases. The unsteady propeller problem is characterized by a typical dipole noise pattern radiating strongest along the propeller axis. The situation in the turbine problem, however, is shown to be quite the opposite, with minimum noise radiating along the turbine axis^{**}. This might be because of the decelerating flow behind the turbine due to its energy

^{**} We need to be careful about this conclusion since we are only looking at the linear noise.

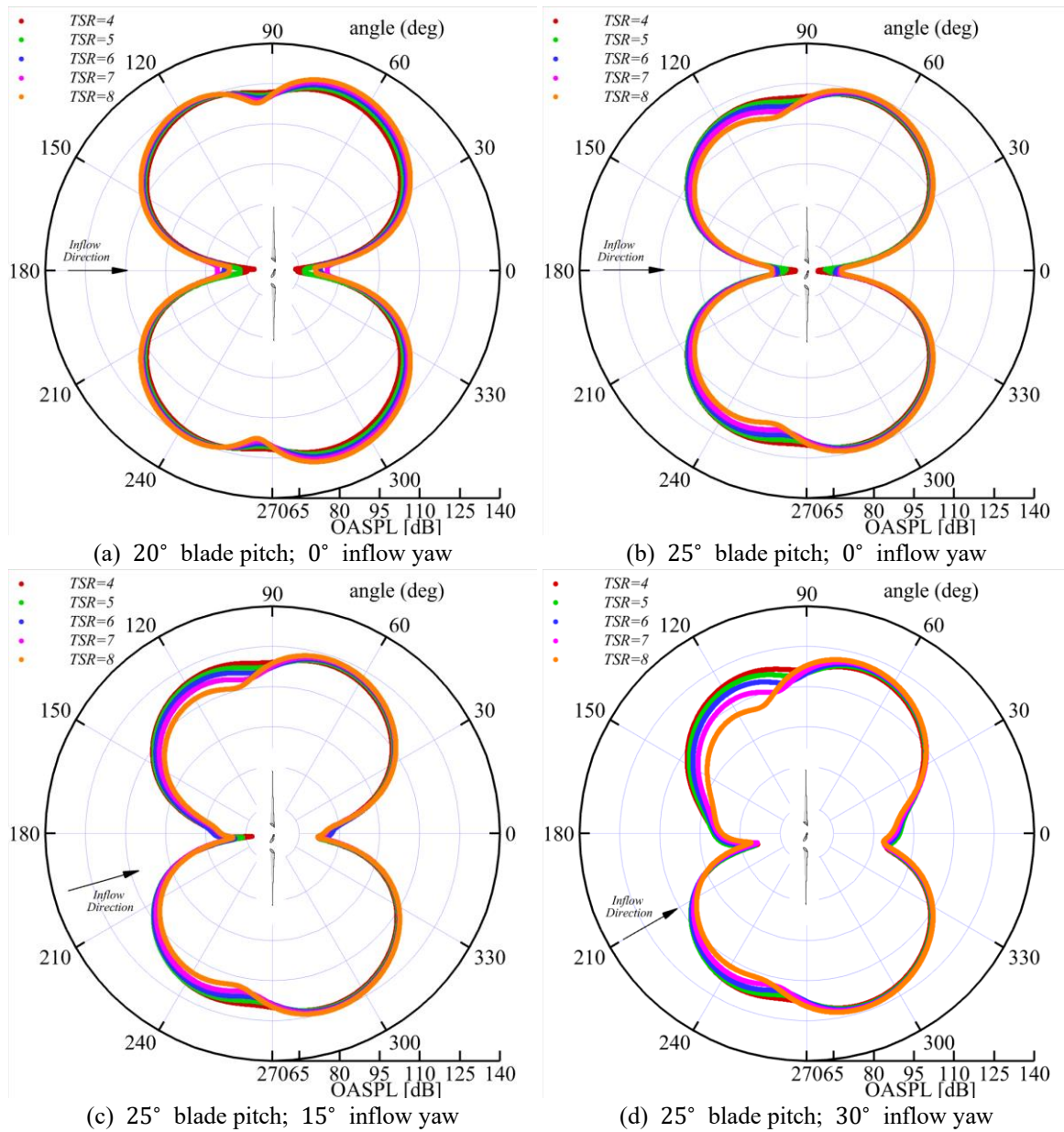


Fig. 10 Noise directivity on the horizontal plane ($y/R = 0.0$) at several TSRs ($c_0 = 1,500$ m/s); pressure transducers are sitting around the turbine at $r/R = 2.0$

harvesting mechanism out of the flow. Lloyd *et al.* (2014) performed high-fidelity LES simulations coupled with FW-H using the same turbine model (15° blade pitch at $TSR = 6$). They reported a similar near-field analysis at $r/R = 4.0$ (our work is done at $r/R = 2.0$ with 20° and 25° blade pitches) of the noise levels around the turbine from $\theta = 0^\circ$ to 90° . Their noise distribution looked quite different from the results shown in this paper – they drew the conclusion that the noise directivity behaved like a monopole rather than a quadrupole. The reason for the difference might

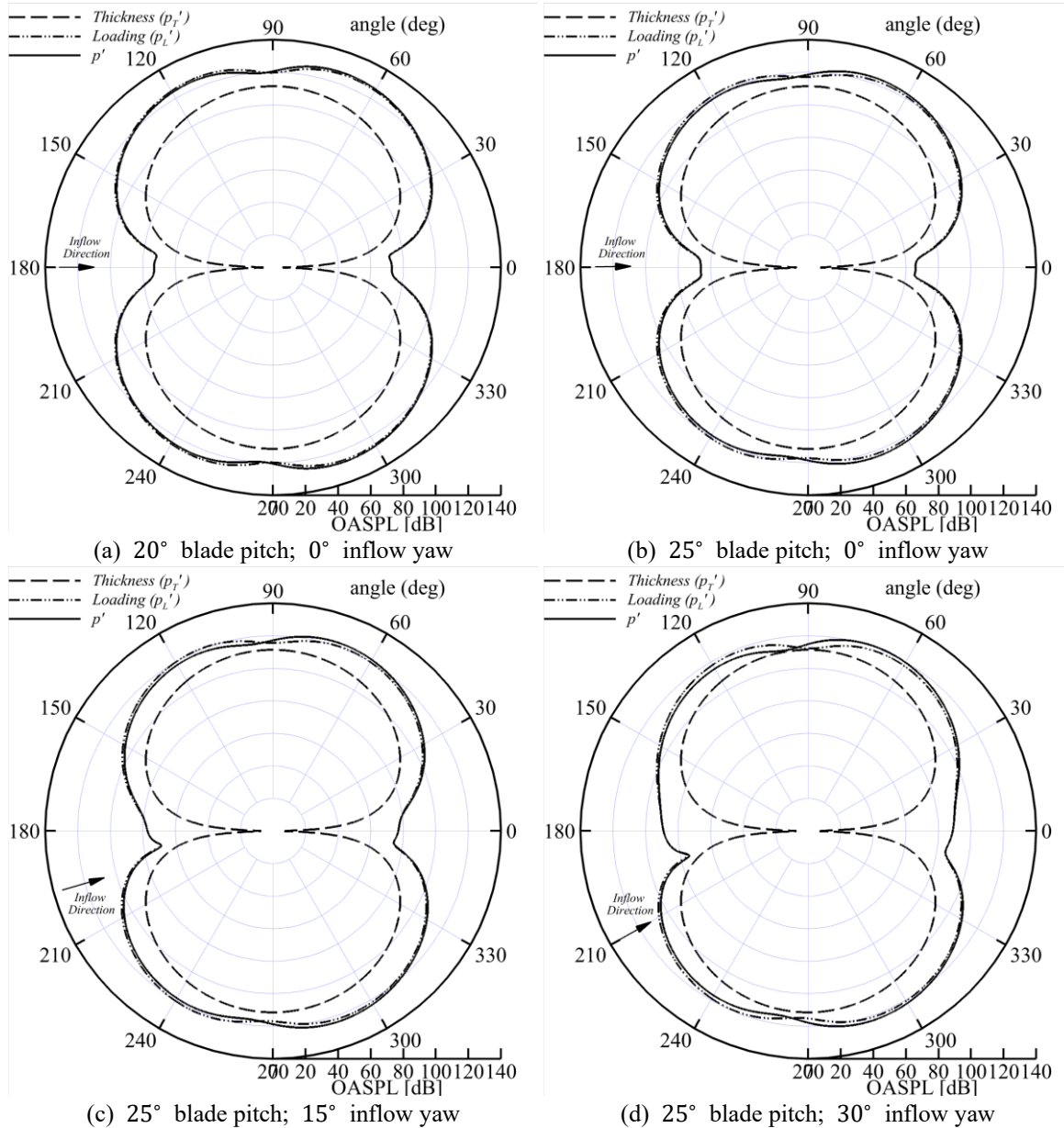


Fig. 11 Noise directivity on the horizontal plane ($y/R = 0.0$) for p_T' , p_L' , and p' at $TSR = 6$ ($c_0 = 1,500$ m/s); pressure transducers are sitting around the turbine at $r/R = 2.0$.

be twofold: one due to the missing quadrupole noise in our study, which is expected to be more pronounced in the downstream direction ($\theta = 0^\circ$), and the other due to the synthetic inflow turbulence that drastically altered the noise generation in their LES simulations. Albeit the FW-H acoustic analogy in their work was performed using only the terms relating to fluid loading (an acoustic dipole), this assumption might not be a leading contributor to the difference from our results because the major noise still originates from the loading noise at $r/R = 2.0$ (Fig. 11).

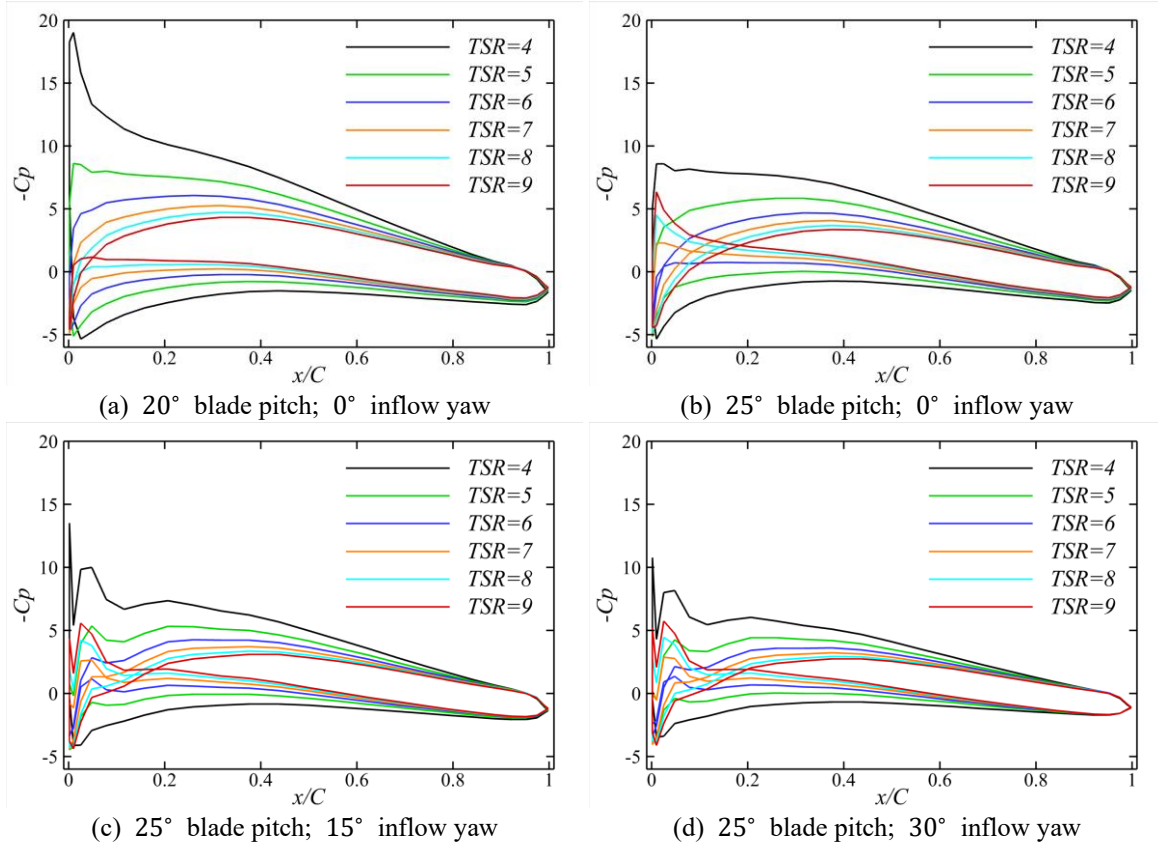


Fig. 12 Pressure distribution on the blade at $r/R = 0.7$ station under various testing conditions

The turbine noise is shown to be sensitive not only to the blade pitch but also to the rotational speed of the blade. When the near-field noise increases with TSR under the uniform inflow with zero yaw (Fig. 10(a)), the directivity patterns show, although the difference is small, the increase in the rotational speed mainly contributes to the downstream noise rather than the other side. The opposite happens if the blade pitch is slightly increased (Fig. 10(b)); the upstream noise in this case decreases faster than the downstream noise with TSR. A possible explanation for the opposite trends might be found in pressure distribution $-C_p$ (Eq. (14)) on the blade (Fig. 12).

$$-C_p = \frac{p_0 - p}{\frac{1}{2}\rho n^2 D^2} \tag{14}$$

where p and p_0 are the predicted blade pressure and the reference pressure far upstream, respectively. Increasing blade pitch from 20° to 25° affects the blade pressure especially near the leading edge. It imposes negative loading with reversed pressures (Figs. 12(b)-12(d)) that become more distinct as TSR increases and consequently can further lower the upstream noise. High pitch puts the blade leading edge more toward the upstream (BEM/FW-H maintains a full description of the 3D geometry), so the upstream noise becomes more sensitive to the negative loading and its change with TSR than the downstream noise.

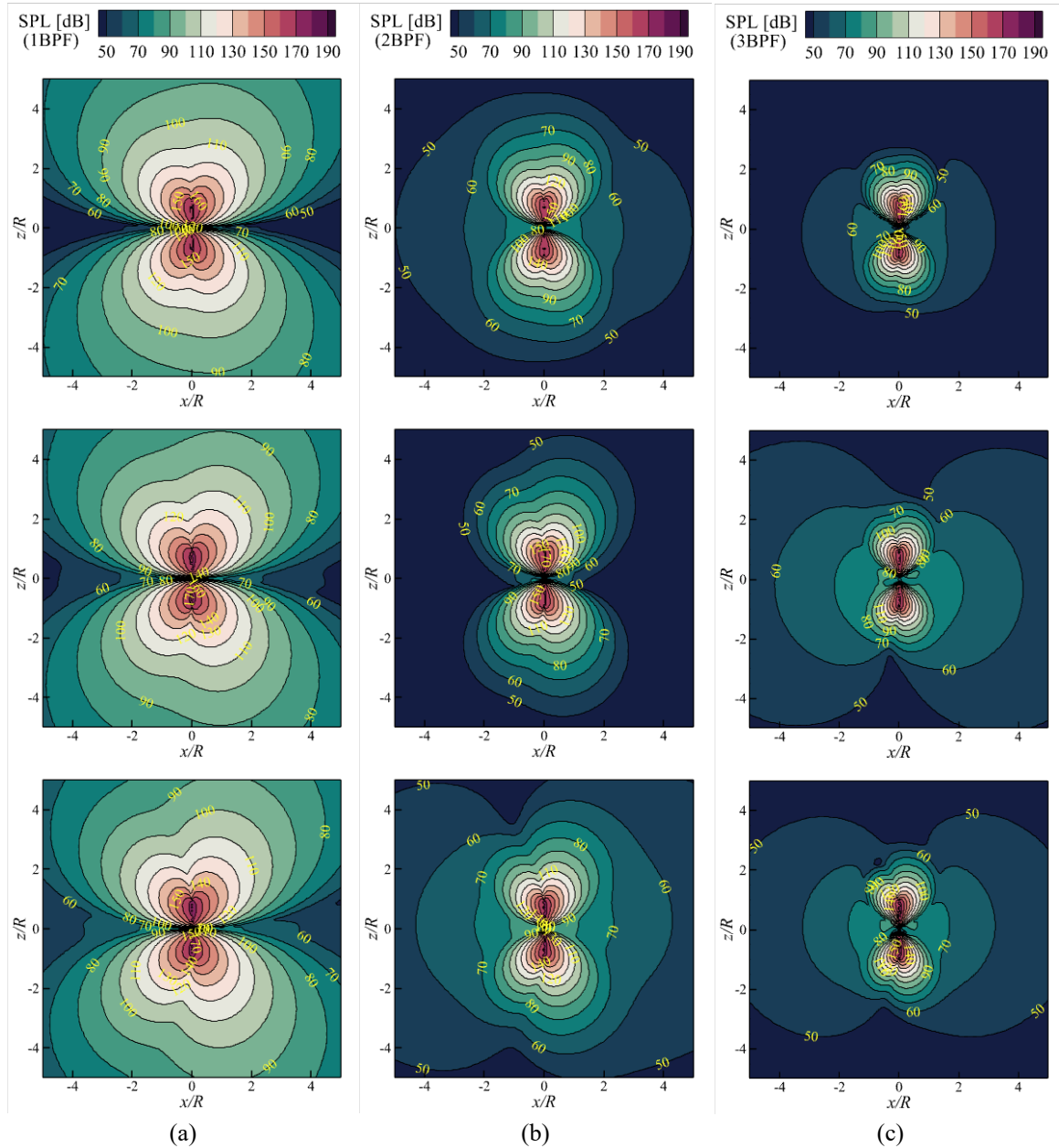


Fig. 13 Contour plots of the sound pressure level at (a) BPF, (b) 2BPF, and (c) 3BPF (dB; *re* $1\mu\text{Pa}$) plotted on the horizontal plane ($y/R = 0.0$) at TSR=(top) 5, (middle) 7, and (bottom) 9; $c_0 = 1,500$ m/s (20° blade pitch; 0° inflow yaw)

In case a non-zero yaw is assumed in inflow, the near-field noise clearly shows asymmetry about the turbine axis. This characteristic is more pronounced at high TSRs. The directivity patterns again confirm that the noise on the starboard side ($\theta = 0^\circ \sim 180^\circ$) behaves more sensitive to the changes in TSR than those on the port side ($\theta = 180^\circ \sim 360^\circ$). It is because the blade pressures on the

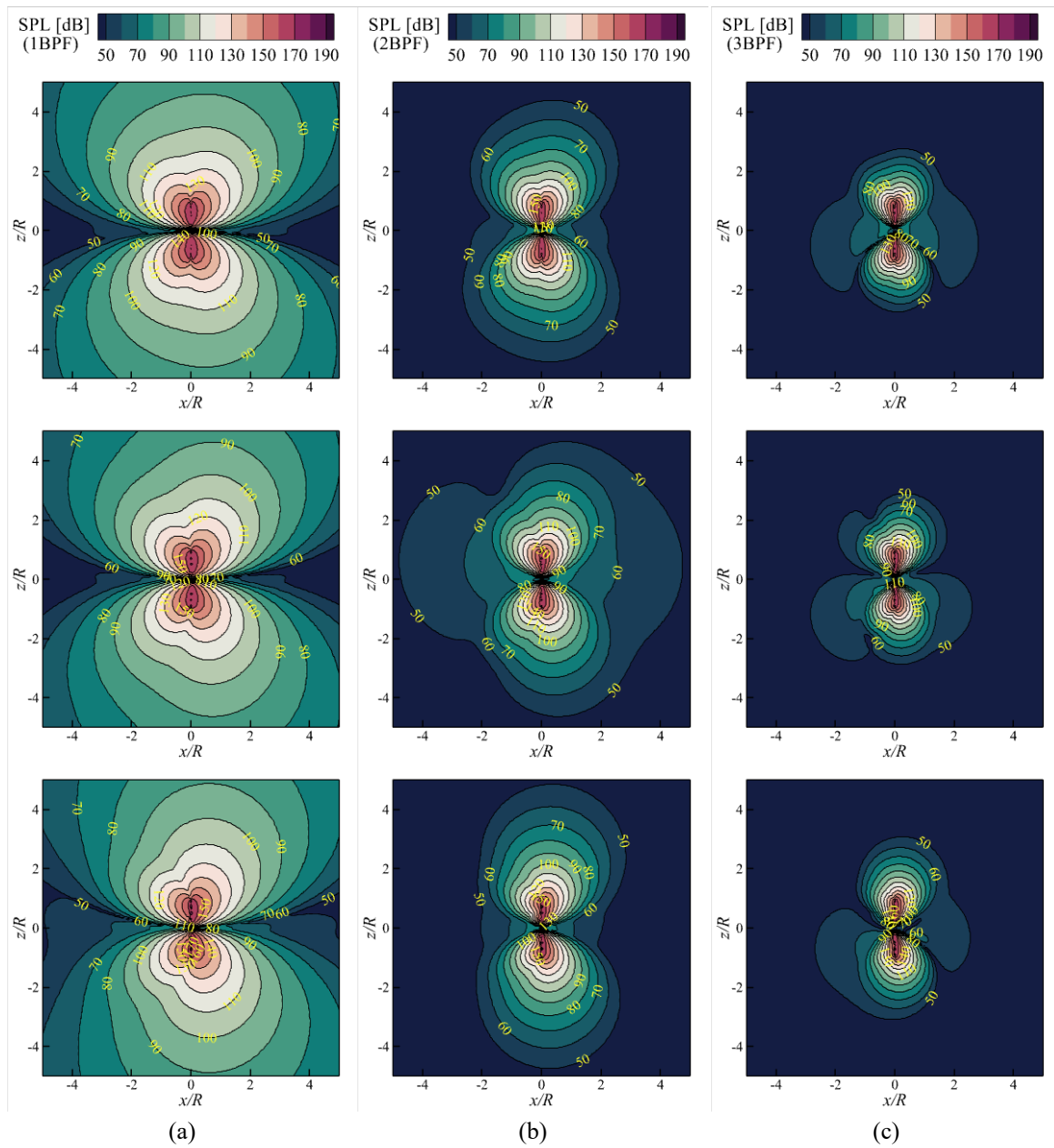


Fig. 14 Contour plots of the sound pressure level at (a) BPF, (b) 2BPF, and (c) 3BPF (dB; *re* $1\mu\text{Pa}$) plotted on the horizontal plane ($y/R = 0.0$) at TSR=(top) 5, (middle) 7, and (bottom) 9; $c_0 = 1,500$ m/s (25° blade pitch; 0° inflow yaw)

starboard side experience more intense reserved pressures than those on the port side under the non-zero yaw conditions, because of which the overall magnitude of the near-field noise also diminishes with TSR.

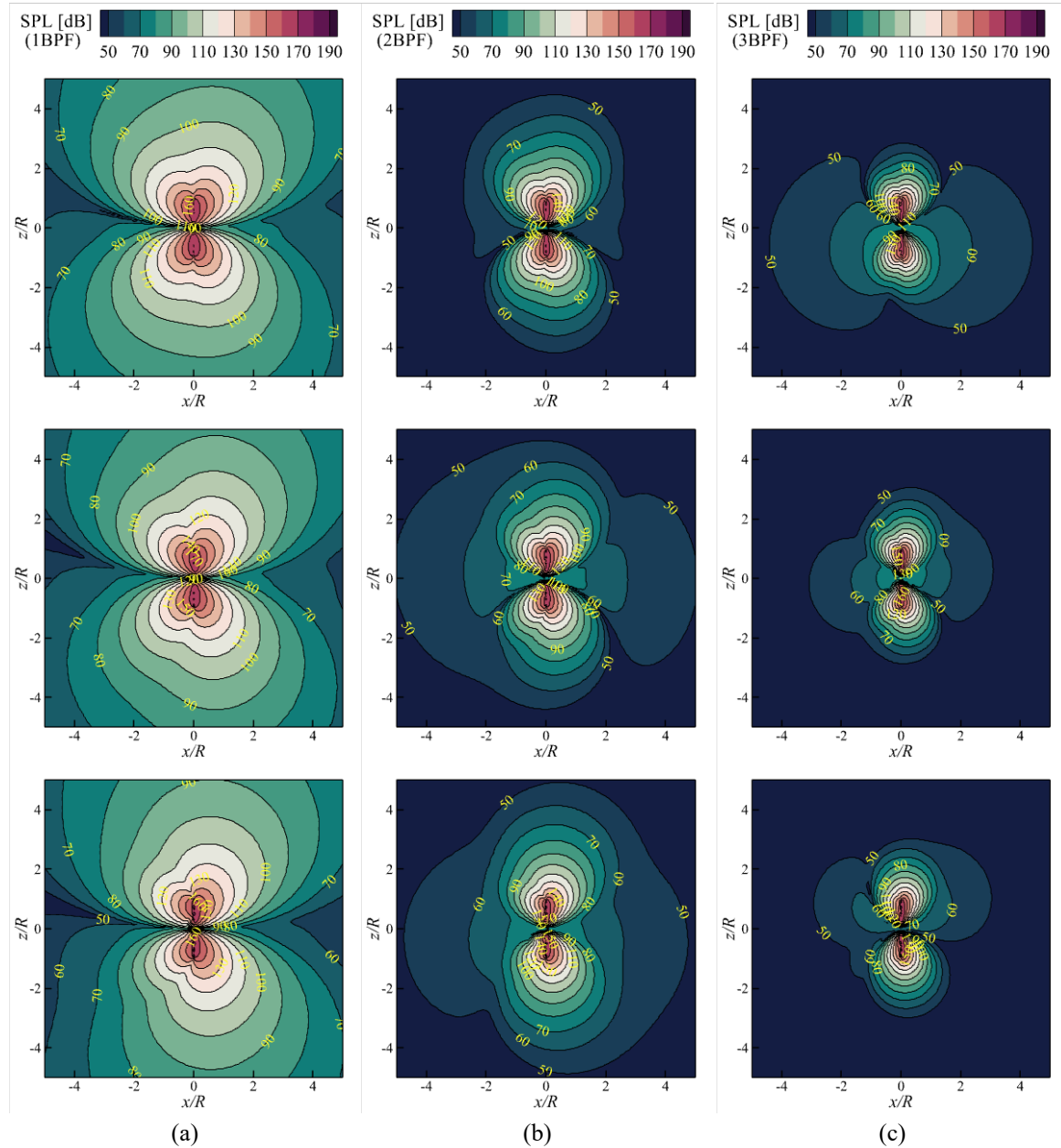


Fig. 15 Contour plots of the sound pressure level at (a) BPF, (b) 2BPF, and (c) 3BPF (dB; *re* $1\mu\text{Pa}$) plotted on the horizontal plane ($y/R = 0.0$) at TSR=(top) 5, (middle) 7, and (bottom) 9; $c_0 = 1,500$ m/s (25° blade pitch; 15° inflow yaw)

Fig. 13 through 16 show the contour plots of the sound pressure levels (dB; *re* $1\mu\text{Pa}$) plotted on the horizontal plane ($y/R = 0.0$) through the turbine center at three different frequencies (i.e., blade passing frequency (BPF), 2BPF, and 3BPF) where most acoustic energy is concentrated. Each figure also includes the results from different TSRs. The overall noise decreases with frequency for

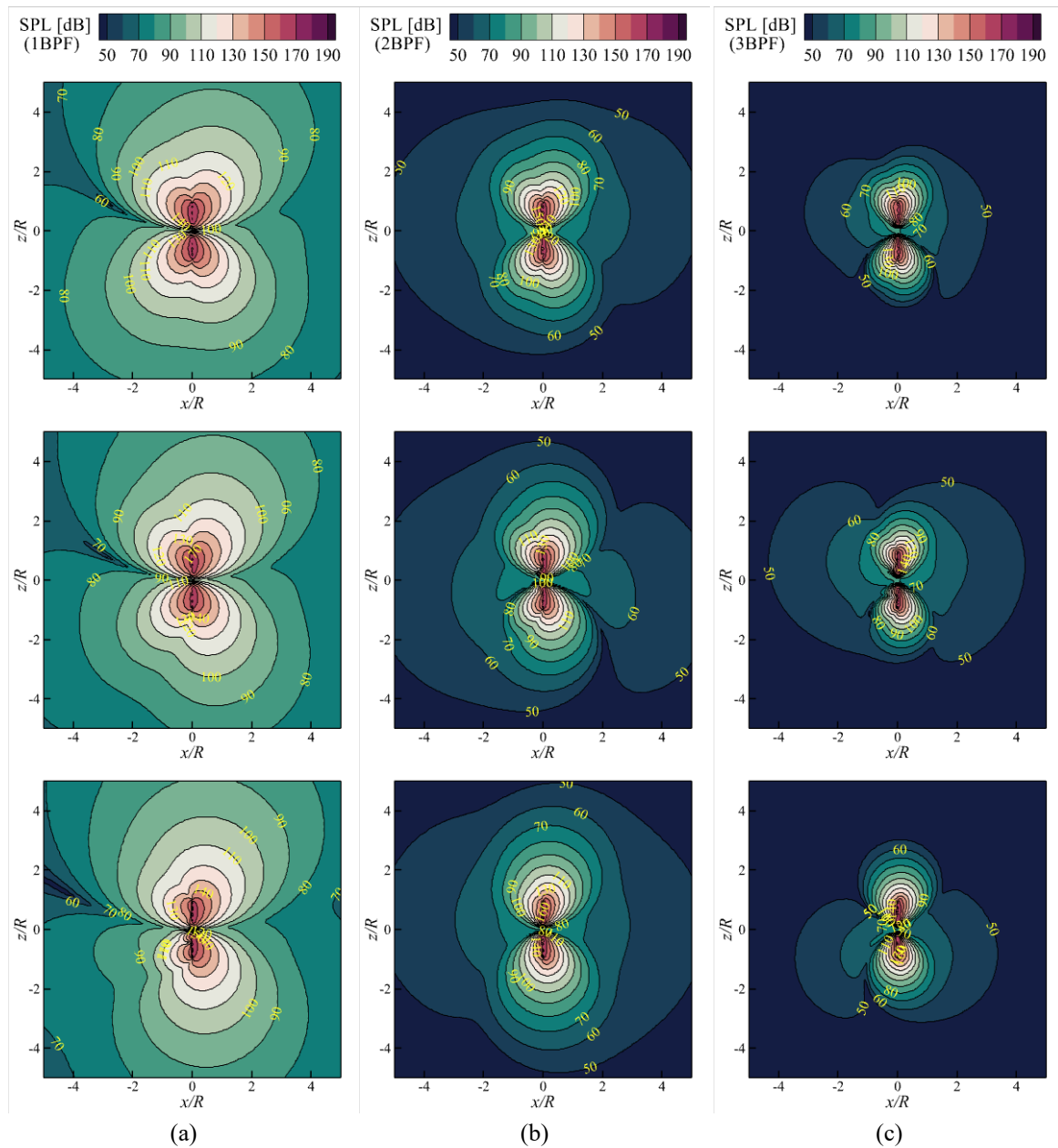


Fig. 16 Contour plots of the sound pressure level at (a) BPF, (b) 2BPF, and (c) 3BPF (dB; *re* $1\mu\text{Pa}$) plotted on the horizontal plane ($y/R = 0.0$) at TSR=(top) 5, (middle) 7, and (bottom) 9; $c_0 = 1,500$ m/s (25° blade pitch; 30° inflow yaw)

all cases regardless of the inflow condition. The SPL contour plots show that the low-pitch case (Fig. 13) produces more noise in both the upstream and downstream directions than the high-pitch case (Fig. 14). The quadrupole noise characteristics are shown to be more pronounced at high TSRs.

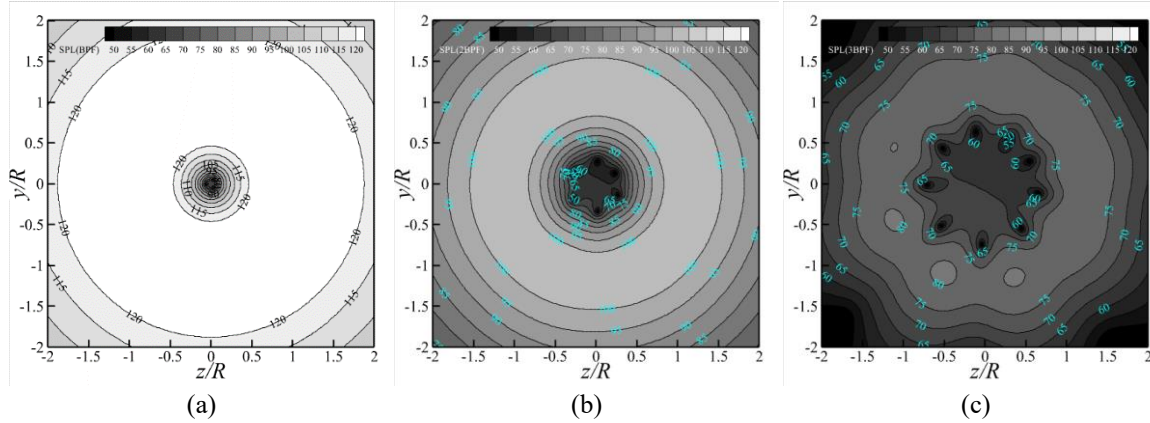


Fig. 17 Contour plots of the sound pressure level at (a) BPF, (b) 2BPF, and (c) 3BPF (dB; *re* 1 μ Pa) plotted on the vertical plane ($x/R = 1.0$) at $TSR = 5$; $c_0 = 1,500$ m/s (25° blade pitch; 0° inflow yaw)

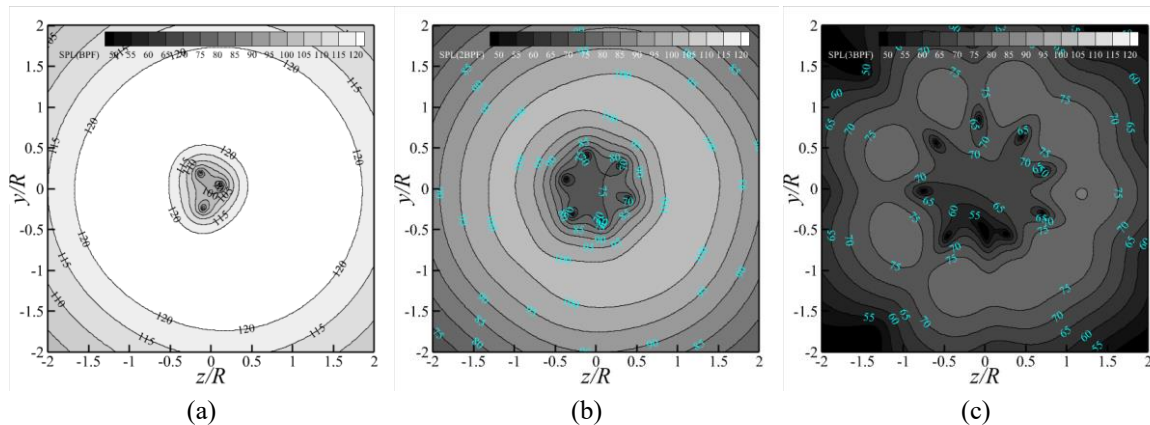


Fig. 18 Contour plots of the sound pressure level at (a) BPF, (b) 2BPF, and (c) 3BPF (dB; *re* 1 μ Pa) plotted on the vertical plane ($x/R = 1.0$) at $TSR = 5$; $c_0 = 1,500$ m/s (25° blade pitch; 30° inflow yaw)

Figs. 17 and 18 show the sound pressure levels up to 3BPF on the vertical plane behind the turbine ($x/R = 1.0$). The 0° and 30° yaw with 25° pitch cases are investigated. For the former, the noise patterns seem to be quite symmetric about the turbine axis. There are distinct troughs in the noise patterns captured in the order of blade number times the blade passing frequency. For the second blade passing frequency, for example, in total six troughs are shown in the contours mainly because of the interference among the radiating noise from each blade. The radial locations of the troughs from the turbine center increase with frequency. Low-frequency noise is generated from most parts of the blade, while high-frequency noise moves radially outward and concentrates relatively at the upper part of the blade. Under 30° yaw (Fig. 18), the predicted noise patterns now start to show distinct asymmetry about the turbine axis because of the inclined inflow. Aligned with the near-field noise directivities (Fig. 10), more noise is produced toward the inflow direction ($z/R > 0.0$) for all frequencies.

5. Conclusions

In this paper, a boundary element method (BEM) is coupled with an acoustic analogy, the Ffowcs Williams-Hawkings (FW-H) equation, to numerically predict the tidal turbine noise under various testing conditions. The primary purpose is to investigate how the noise patterns around the tidal turbine change under different loading or inflow conditions. To this end, the model turbine is selected from a reference case, for which model test experiments were carried out in the cavitation tunnel. The predicted open water performance from the hydrodynamic BEM is first validated against experimental measurements with/without yaw in inflow at several loading conditions. Afterward, the predicted turbine performance is used as the known noise source for the subsequent acoustic analysis based on the BEM/FW-H approach. Throughout the analysis from a hydrodynamic or hydroacoustic point of view, the following conclusions are drawn in this study:

- Without yaw in inflow, a low-pitch blade produces a higher C_F and C_{POW} than a high-pitch blade. There might be a certain critical angle, beyond which this rule does not apply because of the well-known stall phenomenon, so more investigation is needed on the turbine geometry and corresponding performance experimentally and numerically.
- In case the blade pitch is fixed, inclination in inflow lowers both C_F and C_{POW} because of the opposite direction of the inflow and blade motion at certain angular positions; this trend becomes more pronounced as the inclination angle increases.
- Unlike the propeller problem, the tidal turbine radiates the weakest along the turbine axis even under the unsteady flow; it radiates strongest in the side directions with quadrupole noise characteristics, which becomes more distinct at high TSRs.
- The near-field noise predictions reveal that the turbine produces more noise downstream than upstream when subject to uniform inflow. This is because the turbine blade has a negative camber as opposed to the thrusting propeller blade.
- Under the straight inflow aligned to the turbine axis, the turbine noise is sensitive to the change in TSR more on the upstream and downstream directions than the lateral directions.
- Under the inclined flow, noise toward the inflow direction (port side) seems to be less sensitive to TSR than the noise on the starboard side. It is because the blade pressure on the starboard side is more at risk of reversed pressure at the leading edge than on the other side.

Future work includes investigating the turbine-induced noise in a more complex configuration, such as a tidal turbine farm problem. In such a case, it is of practical interest to investigate how the overall noise from each farm configuration differs depending on the relative locations of constituting turbines. Since the inflow direction is not always parallel to the turbine axis in actual situations, looking into the cases where the incoming flow is no longer parallel to the turbine axis would be valuable research within the farm arrangement. Considering the potential effects of cavitation on the turbine-induced noise is also required since the marine turbine is quite vulnerable to cavity inception, which is also known to drop the turbine efficiency significantly. Viscous analysis based on high-fidelity computational fluid dynamics is required to cross-validate the predicted numerical data in various operating conditions. Suitable noise data are sought that preferably maintain a full description of the 3D geometry, high-fidelity noise source without the compactness assumption, and (if possible) all source components of the FW-H formulation for this particular turbine model.

Acknowledgments

Support for this research was provided by the U.S. Office of Naval Research (Grant Number N00014-21-1-2488; Dr. Yin Lu Young) and by Phases VIII and IX of the “Consortium on Cavitation Performance of High-Speed Propulsors.”

References

- Bahaj, A.S., Molland, A.F., Chaplin, J.R. and Batten, W.M.J. (2007), “Power and thrust measurements of marine current turbines under various hydrodynamic flow conditions in a cavitation tunnel and a towing tank”, *Renew. Energ.*, **32**(3), 407-426.
- Baltazar, J., and Falcão de Campos, J.A.C. (2011), “Hydrodynamic analysis of a horizontal axis marine current turbine with a boundary element method”, *J. Offshore Mech. Arct.*, **133**. <http://dx.doi.org/10.1115/1.4003387>.
- Ebrahimi, A., Seif, M.S. and Nouri-Borujerdi, A. (2019), “Hydrodynamic and acoustic performance analysis of marine propellers by combination of panel method and FW-H equations”, *Math. Comput. Appl.*, **24**(81), 1-18.
- Farassat, F. (2007), “Derivation of Formulations 1 and 1A of Farassat: NASA/TM-2007-214853”, *Tech. Rep.*
- Ffowcs-Williams, J.E. and Hawkings, D.L. (1969), “Sound generated by turbulence and surfaces in arbitrary motion”, *Philos. T. R. Soc. Lond. Ser. A Math. Phys. Eng. Sci.*, **264**(1151), 321-341.
- Götttsche, U., Lampe, T., Scharf, M. and Abdel-Maksoud, M. (2019), “Evaluation of underwater sound propagation of a catamaran with cavitating propellers”, *Proceedings of the 6th International Symposium on Marine Propulsors (SMP’19)*, Rome, Italy, May 26-30.
- Haxel, J., Zang, X., Martinez, J., Polagye, B., Staines, G., Deng, Z.D., Wosnik, M. and O’Byrne, P. (2022), “Underwater noise measurements around a tidal turbine in a busy port setting”, *J. Mar. Sci. Eng.*, **10**(5). <http://doi.org/10.3390/jmse10050632>.
- Kerwin, J.E. and Lee, C. (1978), “Prediction of steady and unsteady marine propeller performance by numerical lifting-surface theory”, *Trans. Society of Naval Architects and Marine Engineers: Jersey City, NJ, USA*, **86**, 218-256.
- Kim, S. and Kinnas, S.A. (2022b), “Numerical prediction of propeller-induced noise in open water and ship behind conditions”, *Ocean Eng.*, **261**, 112122. <https://doi.org/10.1016/j.oceaneng.2022.112122>.
- Kim, S. and Kinnas, S.A. (2022c), “Numerical prediction of underwater noise on a flat hull induced by twin or podded propeller systems”, *J. Sound Vib.*, **539**, 117256. <http://doi.org/10.1016/j.jsv.2022.117256>.
- Kim, S., Kumar, K.S. and Kinnas, S.A. (2023), “Hydrodynamic analysis of ducted marine turbine: Study on the duct and turbine efficiency”, *Proceedings of the 28th SNAME Offshore Symposium*, Houston, Texas, Mar. 8.
- Kim, S., Su, Y. and Kinnas, S.A. (2021), “A BEM/RANS interactive method applied to an axial tidal turbine farm”, *J. Ship Res.*, **65**(4), 320-345. <http://dx.doi.org/10.5957/JOSR.04180018>.
- Kim, S., Wu, T.S. and Kinnas, S.A. (2022a), “Design and analysis of tidal turbines via a nonlinear optimization technique coupled with a BEM”, *Proceedings of the 27th SNAME Offshore Symposium*, Houston, Texas, Feb. 22.
- Kinnas, S.A., Yu, X. and Tian, Y. (2012), “Prediction of propeller performance under high loading conditions with viscous/inviscid Interaction and a new wake alignment model”, *Proceedings of the 29th Symposium on Naval Hydrodynamics*, Gothenburg, Sweden, Aug. 26-31.
- Lloyd, T.P. (2013), “Large eddy simulations of inflow turbulence noise: application to tidal turbines”, Ph.D. Dissertation, University of Southampton, United Kingdom.
- Lloyd, T.P., Turnock, S.R. and Humphrey, V.F. (2014), “Assessing the influence of inflow turbulence on noise and performance of a tidal turbine using large eddy simulations”, *Renew. Energ.*, **71**, 742-754. <https://doi.org/10.1016/j.renene.2014.06.011>.

- Lossent, J., Lejart, M., Folegot, T., Clorennec, D., Di Iorio, L. and Gervaise, C. (2018), "Underwater operational noise level emitted by a tidal current turbine and its potential impact on marine fauna", *Mar. Pollut. Bull.*, **131**, 323-334. <https://doi.org/10.1016/j.marpolbul.2018.03.024>.
- Menéndez Arán, D.H., Tian, Y. and Kinnas, S.A. (2019), "Effect of wake Alignment on turbine blade loading distribution and power coefficient", *J. Offshore Mech. Arct.*, **141**(4). <http://dx.doi.org/10.1115/1.4041669>.
- Otto, W., Rijpkema, D. and Vaz, G. (2012), "Viscous-flow calculations on an axial marine current turbine", *Proceedings of the ASME 2012 31st International Conference on Ocean, Offshore and Arctic Engineering*, Rio de Janeiro, Brazil, July 1-6.
- Risch, D., van Geel, N., Gillespie, D. and Wilson, B. (2020), "Characterisation of underwater operational sound of a tidal stream turbine", *J. Acoust. Soc. Am.*, **147**(4). <http://doi.org/10.1121/10.0001124>.
- Schmitt, P., Elsaesser, B., Coffin, M., Hood, J. and Starzmann, R. (2015), "Field testing a full-scale tidal turbine Part 3: Acoustic characteristics", *Proceedings of the 11th European Wave and Tidal Energy Conference*, Nantes, France, Sept. 9.
- Seol, H., Jung, B., Suh, J. and Lee, S. (2002), "Prediction of non-cavitating underwater propeller noise", *J. Sound Vib.*, **257**(110), 131-156.
- Shi, W., Atlar, M., Rosli, R., Aktas, B. and Norman, R. (2016), "Cavitation observations and noise measurements of horizontal axis tidal turbines with biomimetic blade leading-edge designs", *Ocean Eng.*, **121**, 143-155. <https://doi.org/10.1016/j.oceaneng.2016.05.030>.
- Testa, C., Lanniello, S. and Salvatore, F. (2018), "A Ffowcs Williams and Hawkings formulation for hydroacoustic analysis of propeller sheet cavitation", *J. Sound Vib.*, **413**, 421-441.
- Wu, T. S., Kim, S. and Kinnas, S. A. (2023), "Numerical prediction of skin friction coefficient by coupling a BEM with X-Foil: Effect on the hydrofoil and propeller performance", *Proceedings of the 28th SNAME Offshore Symposium*, Houston, Texas, Mar. 8.
- Young, Y.L., Motley, M.R. and Yeung, R.W. (2010), "Three-dimensional numerical modeling of the transient fluid-structural interaction response of tidal turbines", *J. Offshore Mech. Arct.*, **132**(1). <http://doi.org/10.1115/1.3160536>.

Appendix A. Selection of the friction coefficient over the blade

C_f in this work is calculated according to the ITTC-1957 friction correlation line

$$C_f(r) = \frac{0.075}{(\log_{10} Re_{local}(r)-2)^2}, \quad (\text{A.1})$$

where $Re_{local}(r)$ is the local Reynolds number (Eq. (A.2)) calculated at each station of the blade based on the radial location r of the station, local inflow including rotational component, and global Reynolds number $Re_{global} = 1e6$ given for the cases we looked at

$$Re_{local}(r) = Re_{global} \frac{\sqrt{V(r)^2 + \omega^2 r^2} c(r)}{V_R D}, \quad (\text{A.2})$$

$$Re_{global} = \frac{V_R D}{\nu}, \quad (\text{A.3})$$

where $V(r)$ is the local inflow; $c(r)$ the local chord; D the diameter of the turbine blade; ν the kinematic viscosity; and $V_R = \sqrt{V_{up}^2 + (0.7n\pi D)^2}$ is the reference velocity with V_{up} being the inflow speed far upstream.

Each station is considered independent, and the influence from neighboring stations is ignored during the calculation. Predicted $Re_{local}(r)$ and $C_f(r)$ are in a function of radial distance from the blade center and given constant over the respective station. Fig. A.1 shows the predicted $Re_{local}(r)$ and $C_f(r)$ for the turbine with 25° pitch and 0° yaw at $TSR = 6$. The range of $C_f(r)$ in this case is predicted $.0072 < C_f(r) < .0082$, based on which the present work selected a constant $C_f = .008$ (over the entire blade surface) that allows the most reliable and stable BEM predictions.

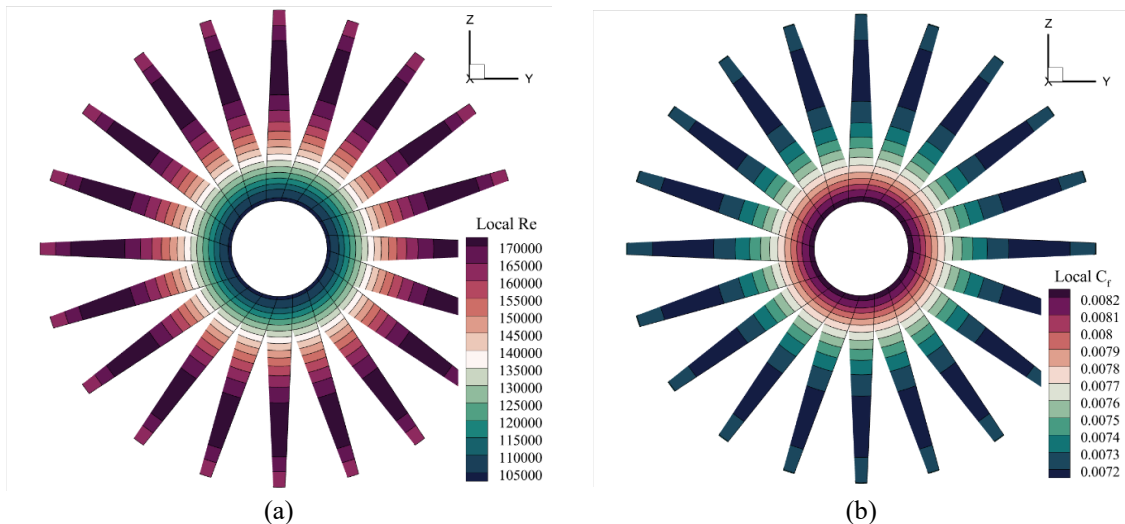


Fig. A.1 Predicted (a) local Reynolds number and corresponding (b) local friction coefficients based on the ITTC-1957 friction correction line; 25° blade pitch, 0° inflow yaw, and $TSR = 6$.